

A Level Set Approach to a Unified Model for Etching, Deposition, and Lithography II: Three-Dimensional Simulations

D. ADALSTEINSSON AND J. A. SETHIAN*

Department of Mathematics and Lawrence Berkeley Laboratory, University of California, Berkeley, California 94720

We apply a level set formulation to the problem of surface advancement in three-dimensional topography simulation of deposition, etching, and lithography processes in integrated circuit fabrication. The level set formulation is based on solving a Hamilton–Jacobi-type equation for a propagating level set function, using techniques borrowed from hyperbolic conservation laws. Topological changes, corner and cusp development, and accurate determination of geometric properties such as curvature and normal direction are naturally obtained in this setting. The equations of motion of a unified model, including the effects of isotropic and unidirectional deposition and etching, visibility, surface diffusion, reflection, and material dependent etch/deposition rates are presented and adapted to a level set formulation. In Part I of this paper, the basic equations and algorithms for two-dimensional simulations were developed. In this paper, the extension to three dimensions is presented. We show a large collection of simulations, including three-dimensional etching and deposition into cavities under the effects of visibility, directional and source flux functions, evolution of lithographic profiles, discontinuous etch rates through multiple materials, and non-convex sputter yield flux functions. In Part III of this paper, effects of reflection and re-emission and surface diffusion will be presented. © 1995 Academic Press, Inc.

1. INTRODUCTION

In this paper, we continue the development of a level set formulation to simulated deposition, etching, and lithography in integrated circuit fabrication. The goal is an accurate, stable, and efficient technique for surface advancement due to complex motion which, under different physical effects, may include effects of anisotropy, visibility conditions, and material-dependent propagation rates. In Part I of this paper, “A Level Set Approach to a Unified Model for Etching, Deposition, and Photolithography I: Two-Dimensional Simulations” [2], the basic equations and algorithms for two-dimensional simulations are developed. In this paper, the extension to three dimensions is presented. We show a large collection of simulations, including three-dimensional etching and deposition into cavities under the effects of visibility, directional and

source flux functions, evolution of lithographic profiles, discontinuous etch rates through multiple materials, and non-convex sputter yield flux functions. The validity of various physical models for microfabrication will not be examined. Instead, we hope to provide a robust numerical approach to these phenomena which can then be used to systematically examine various models.

A variety of numerical algorithms are available to advance fronts in etching, deposition and photolithography processes. These methods are not unique to such simulations and, in fact, are in use in such areas as dendritic growth and solidification, flame/combustion models, and fluid interfaces. Roughly speaking, they fall into three general categories:

- *Marker/string methods.* In these methods, a discrete parametrized version of the interface boundary is used. In two dimensions, marker particles are used; in three dimensions, a nodal triangularization of the interface is often developed. The positions of the nodes are then updated by determining front information about the normals and curvature from the marker representation. Such representations can be quite accurate, however, limitations exist for complex motions. To begin, if corners and cusps develop in the evolving front, markers usually form “swallow-tail” solutions which must be removed through delooping techniques which attempt to enforce an entropy condition inherent in such motion (see [34]). Second, topological changes are difficult to handle; when regions merge, some markers must be removed. Third, significant instabilities in the front can result, since the underlying marker particle motions represent a weakly ill-posed initial value problem (see [26]). Finally, extensions of such methods to three dimensions require additional work.

- *Cell-based methods.* In these methods, the computational domain is divided into a set of cells which contain “volume fractions.” These volume fractions are numbers between 0 and 1 and represent the fraction of each cell containing the physical material. At any time, the front can be reconstructed from these volume fractions. Advantages of such techniques include the ability to easily handle topological changes, design adaptive mesh methods, and

* Supported in part by the Applied Mathematics Subprogram of the Office of Energy Research under Contract DE-AC03-76SF00098 and the National Science Foundation and DARPA under Grant DMS-8919074.

build extensions to three dimensions. However, determination of geometric quantities such as normals and curvature can be inaccurate.

- *Characteristic Methods.* In these methods, “ray-trace”-like techniques are used. The characteristic equations for the propagating interface are used, and the entropy condition at forming corners (see [34]) is formally enforced by constructing the envelope of the evolving characteristics. Such methods handle the looping problems more naturally, but may be complex in three-dimensions and require the adaptive addition and removal rays, which can cause instabilities and/or oversmoothing.

Level set methods, introduced in [26], offer highly robust and accurate methods for tracking interfaces moving under complex motions. Their major virtue is that they naturally construct the fundamental weak solution to surface propagation posed by Sethian [33, 34]. They work in any number of space dimensions, naturally handle topological merging and breaking naturally, and are easy to program. They approximate the equation of motion for the underlying propagating surface, which resembles Hamilton–Jacobi equations with parabolic right-hand sides. The central mathematical idea is to view the moving front as a particular level set of a higher dimensional function. In this setting, sharp gradients and cusps can form easily, and the effects of curvature may be easily incorporated. The key numerical idea is to borrow technology from the numerical solution of hyperbolic conservation laws and transfer these ideas to the Hamilton–Jacobi setting, which then guarantees that the correct entropy satisfying solution will be obtained.

In Part I of this paper [2], the level set technique was used to develop detailed two-dimensional calculations of etching, deposition, and lithography problems. The resulting numerical method accurately predicts two-dimensional profile evolution, naturally taking into account such effects as incident angles, masks, yield functions, visibility, and anisotropy on the surface motion. Due to the use of conservative upwind schemes, the method selects the correct weak solution; where shocks in the tangent occur, the necessary entropy condition is invoked; at outward-facing corners the correct rarefaction fan solution is built. The method is second-order accurate in the motion of the front and is of the same computational work as cell and marker particle methods; that is, the work is a constant times the number of points which characterize the evolving front.

We refer the interested reader to Part I of this paper [2] for complete details of the method. In that work, numerical convergence studies and validation tests of the method were performed. Here, we concentrate on the extension to three dimensions and on numerical simulations. The extension of this method to three dimen-

sions requires considerable care in several areas. First, the calculation of visibility is more intricate and time-consuming. Second, an efficient re-initialization of the level set function requires a different algorithm. Third, integration of the flux from the source warrants fast integration techniques.

The outline of this paper is as follows. In Section I, we describe the basic level set algorithm applied to propagating interfaces. In Section II, we give a unified set of equations for the motion of an interface under deposition, etching, and lithography. In Section III, we reformulate these equations in a level set perspective. In Section IV, we discuss some details of the numerical implementation. In Section V, we demonstrate the power of the approach through a series of model problems, and in Section VI we apply the method to some particular problems of interest. Part III of this paper will include the effects of reflection/re-emission and surface diffusion.

2. NUMERICAL ALGORITHMS FOR PROPAGATING FRONTS

2.1. Entropy Conditions and Curvature

The fundamental aspects of front propagation in our context can be illustrated as follows. Let $\gamma(0)$ be a smooth, closed initial curve in R^2 , and let $\gamma(t)$ be the one-parameter family of curves generated by moving $\gamma(0)$ along its normal vector field with speed $F(K)$. Here, $F(K)$ is a given scalar function of the curvature K . Thus, $n \cdot x_t = F(K)$, where x is the position vector of the curve, t is time, and n is the unit normal to the curve.

Consider a speed function of the form $1 - \varepsilon K$, where ε is a constant. An evolution equation for the curvature K (see [34]) is given by

$$K_t = \varepsilon K_{\alpha\alpha} + \varepsilon K^3 - K^2, \quad (1)$$

where we have taken the second derivative of the curvature K with respect to arclength α . This is a reaction-diffusion equation; the drive toward singularities due to the reaction term ($\varepsilon K^3 - K^2$) is balanced by the smoothing effect of the diffusion term ($\varepsilon K_{\alpha\alpha}$). Indeed, with $\varepsilon = 0$, we have a pure reaction equation $K_t = -K^2$. In this case, the solution is $K(s, t) = K(s, 0)/(1 + tK(s, 0))$, which is singular in finite t if the initial curvature is anywhere negative. Thus, corners can form in the moving curve when $\varepsilon = 0$.

As an example, consider the periodic initial cosine curve

$$\gamma(0) = (-s, [1 + \cos 2\pi s]/2) \quad (2)$$

propagating with speed $F(K) = 1 - \varepsilon K$, $\varepsilon > 0$. As the front moves, the troughs at $s = n + \frac{1}{2}$, $n = 0, \pm 1, \pm 2, \dots$ are sharpened by the negative reaction term (because

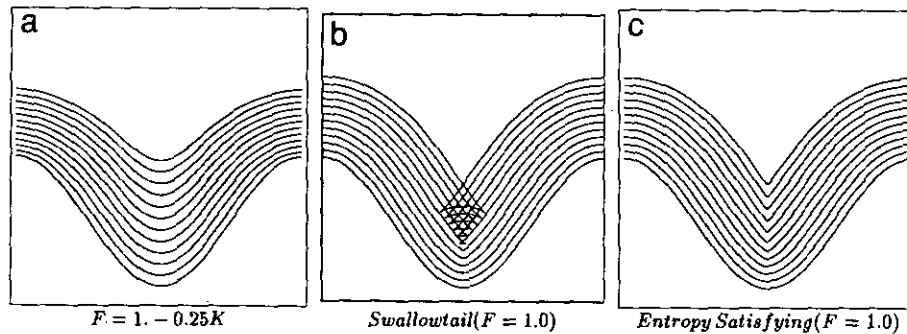


FIG. 1. Propagating cosine curve.

$K < 0$ at such points) and smoothed by the positive diffusion term (see Fig. 1a). For $\varepsilon > 0$, it can be shown (see [34, 26]) that the moving front stays C^∞ .

On the other hand, for $\varepsilon = 0$, the front develops a sharp corner in finite time as discussed above. In general, it is not clear how to construct the normal at the corner and continue the evolution, since the derivative is not defined. One possibility is the “swallowtail” solution formed by letting the front pass through itself (see Fig. 1b). However, from a geometrical argument it seems clear that the front at time t should consist of only the set of all points located a distance t from the initial curve. (This is known as the Huygens principle construction, see [34]). Roughly speaking, we want to remove the “tail” from the “swallowtail.” In Fig. 1c, we show this alternate weak solution. Another way to characterize this weak solution is through the following “entropy condition” posed by Sethian (see [34]): If the front is viewed as a burning flame, then *once a particle is burnt it stays burnt*. Careful adherence to this stipulation produces the Huygens principle construction. Furthermore, this physically reasonable weak solution is the formal limit of the smooth solutions as the curvature term vanishes (see [34]).

As further illustration, we consider the case of a V-

shaped front propagating normal to itself with unit speed ($F = 1$). In [33], the link between this motion and hyperbolic conservation laws is explained. In Fig. 2a, the point of the front is downwards; as it moves inwards with unit speed, a shock develops as the front pinches off and an entropy condition is required to select the correct solution and produce the limit of the viscous case. Conversely, in Fig. 2b, the point of the front is upwards; in this case, the unit normal speed results in a rarefaction fan which connects the left state with slope $+1$ to the right state which has slope -1 . Extensive discussion of the role of shocks and rarefactions in propagating fronts may be found in [33].

The key to constructing numerical schemes which adhere to this entropy condition and rarefaction structure comes from the link between propagating fronts and hyperbolic conservation laws. Consider the initial front given by the graph of $f(x)$, with f periodic on $[0, 1]$, and suppose that the propagating front remains a function for all time. Let ϕ be the height of the propagating function at time t , thus $\phi(x, 0) = f(x)$. The tangent at (x, ϕ) is $(1, \phi_x)$, and the equation of motion becomes $\phi_t = F(K)(1 + \phi_x^2)^{1/2}$. Using the speed function $F(K) = 1 - \varepsilon K$ and the formula $K = -\phi_{xx}/(1 + \phi_x^2)^{3/2}$, we get

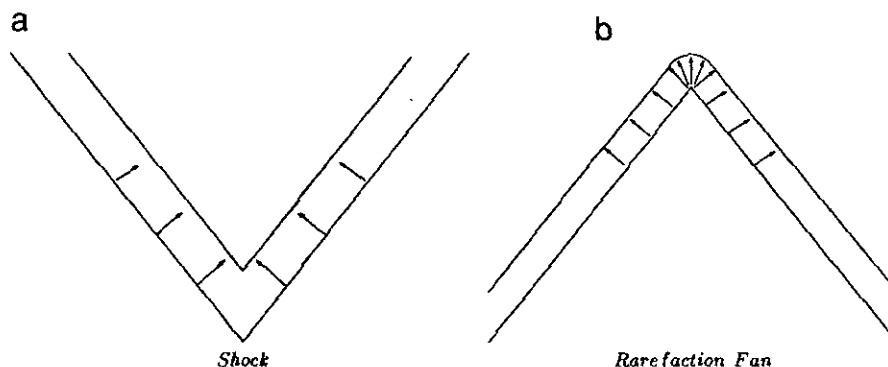


FIG. 2. Front propagating with unit normal speed.

$$\phi_t - (1 + \phi_x^2)^{1/2} = \varepsilon \frac{\phi_{xx}}{1 + \phi_x^2}. \quad (3)$$

Differentiating both sides of this equation yields an evolution equation for the slope $u = d\phi/dx$ of the propagating front, namely

$$u_t + [-(1 + u^2)^{1/2}]_x = \varepsilon \left[\frac{u_x}{1 + u^2} \right]_x. \quad (4)$$

Thus, the derivative of the Hamilton–Jacobi equation with parabolic right-hand side for the changing height ϕ is a viscous hyperbolic conservation law for the propagating slope u (see [37]). Our entropy condition is in fact equivalent to the one for propagating shocks in hyperbolic conservation laws. Thus, we exploit the numerical technology from hyperbolic conservation laws to build consistent, upwind schemes which select the correct entropy condition. For details, see [26, 36].

Our goal then is to use the above equations to develop numerical techniques for propagating fronts. Before doing so, we must extend the above ideas to include propagating fronts which are not easily written as functions. This is the level set idea introduced by Osher and Sethian [26].

2.2. Level Set Methods

Given a moving closed hypersurface $\Gamma(t)$, that is, $\Gamma(t = 0) : [0, \infty) \rightarrow R^N$, we wish to produce an Eulerian formulation for the motion of the hypersurface propagating along its normal direction with speed F , where F can be a function of various arguments, including the curvature, normal direction, etc. The main idea is to embed this propagating interface as the zero level set of a higher dimensional function ϕ . Let $\phi(x, t = 0)$, where $x \in R^N$, be defined by

$$\phi(x, t = 0) = \pm d, \quad (5)$$

where d is the distance from x to $\Gamma(t = 0)$, and the plus (minus) sign is chosen if the point x is outside (inside) the initial hypersurface $\Gamma(t = 0)$. Thus, we have an initial function $\phi(x, t = 0) : R^N \rightarrow R$ with the property that

$$\Gamma(t = 0) = (x | \phi(x, t = 0) = 0). \quad (6)$$

Our goal is to now produce an equation for the evolving function $\phi(x, t)$ which contains the embedded motion of $\Gamma(t)$ as the level set $\phi = 0$. Let $(x(t), t)$ be the path of a point on the propagating front. That is, $x(t = 0)$ is a point on the initial front $\Gamma(t = 0)$, and $\alpha_t \cdot n = F(x(t))$. Since the evolving function ϕ is always zero on the propagating hypersurface, we must have

$$\phi(x(t), t) = 0. \quad (7)$$

By the chain rule,

$$\phi_t + \nabla \phi(x(t), t) \cdot x'(t) = 0. \quad (8)$$

Since $n = F$ where $n = \nabla \phi / |\nabla \phi|$, we then have the evolution equation for ϕ , namely

$$\phi_t + F|\nabla \phi| = 0 \quad (9)$$

$$\phi(x, t = 0) \text{ given.} \quad (10)$$

This is suggestive of a Hamilton–Jacobi equation because, for certain forms of the speed function F , we obtain the standard Hamilton–Jacobi equation.

In Fig. 3 (taken from [35]), we show the outward propagation of an initial curve and the accompanying motion of the level set function ϕ . In Fig. 3a, we show the initial circle, and in Fig. 3c we show the circle at a later time. In Fig. 3b, we show the initial position of the level set function ϕ , and in Fig. 3d, we show this function at a later time.

There are four major advantages to this Eulerian Hamilton–Jacobi formulation. The first is that the evolving function $\phi(x, t)$ always remains a function as long as F is smooth. However, the level surface $\phi = 0$ and, hence, the propagating hypersurface $\Gamma(t)$, may change topology, break, merge, and form sharp corners as the function ϕ evolves (see [26]).

The second major advantage of this Eulerian formulation concerns numerical approximation. Because $\phi(x, t)$ remains a function as it evolves, we may use a discrete grid in the domain of x and substitute finite difference approximations for the spatial and temporal derivatives. In fact, a key aspect to the level set approach is to exploit the technology of hyperbolic conservation laws to construct the correct entropy-satisfying solution.

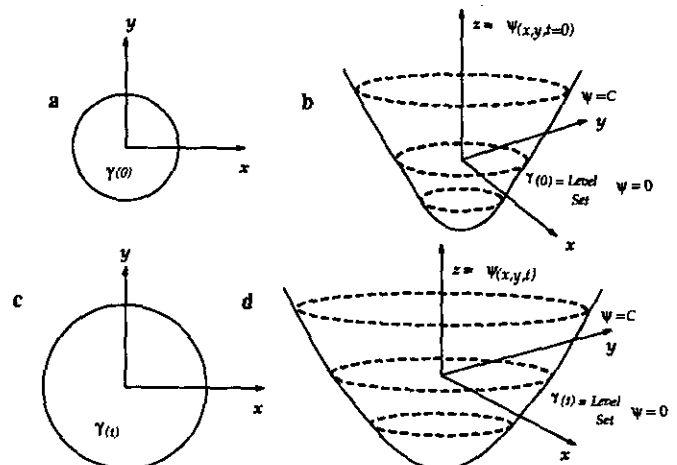


FIG. 3. Propagating circle.

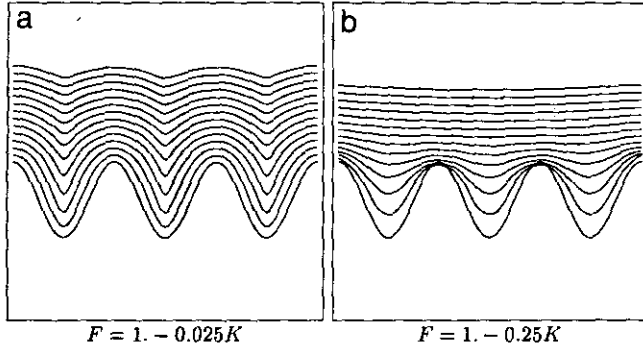


FIG. 4. Propagating triple sine curve: (a) $F = 1 - 0.025K$; (b) $F = 1 - 0.25K$.

The third major advantage of the above formulation is that intrinsic geometric properties of the front may be easily determined from the level set function ϕ . For example, at any point of the front, the normal vector is given by

$$n = \frac{\nabla \phi}{|\nabla \phi|} \quad (11)$$

and the curvature is easily obtained from the divergence of the gradient of the unit normal vector to front, i.e.,

$$K = \nabla \cdot \frac{\nabla \phi}{|\nabla \phi|} = - \frac{\phi_{xx}\phi_y^2 - 2\phi_x\phi_y\phi_{xy} + \phi_{yy}\phi_x^2}{(\phi_x^2 + \phi_y^2)^{3/2}}. \quad (12)$$

Finally, the fourth major advantage of the above level set approach is that there are no significant changes required to follow fronts in three space dimensions. By simply extending the array structures and gradient operators, propagating surfaces are easily handled.

As an example of the application of level set methods, consider once again the problem of a front propagating with speed $F(K) = 1 - \varepsilon K$. In Fig. 4, we show two cases of a propagating initial triple sine curve. For ε small (Fig. 4a), the troughs sharpen up and will result in transverse lines that come too close together. For ε large (Fig. 4b), parts of the boundary with high values of positive curvature can initially move downwards, and concave parts of the front can move quickly upwards.

Since its introduction in [26], the above level set approach has been used in a wide collection of problems involving moving interfaces. Some of these applications include the generation of minimal surfaces [8], singularities and geodesics in moving curves and surfaces [9], flame propagation [29, 44], fluid interfaces [5, 6, 25], and shape reconstruction [22]. Extensions of the basic technique include fast methods [1], grid generation [35], and algorithms for multiple materials [32]. The fundamental Eulerian perspective presented by this approach has since been

adopted in theoretical analysis of mean curvature flow; see, in particular, [11, 7] and related work in [4, 10, 12–14, 17].

3. EQUATIONS OF MOTION FOR DEPOSITION, ETCHING, AND LITHOGRAPHY

We now build the speed function F for deposition, etching, and lithography for the level set equation of motion

$$\phi_t + F|\nabla \phi| = 0 \quad (13)$$

$$\phi(x, t = 0) \text{ given.} \quad (14)$$

Note that F is the speed in the normal direction. Our approach is to write the normal speed function as the superposition of the three main physical effects:

$$F = F_{\text{Deposition}} + F_{\text{Etching}} + F_{\text{Lithography}}. \quad (15)$$

All effects do not take place at once; however, the design of the numerical algorithm allows various combinations of terms to be “turned on” during the surface profile advancement.

The underlying physical effects involved in etching, deposition, and lithography are quite complex; much of the following summary is obtained from the excellent overviews in [30, 31, 41, 42, 23, 28]. The effects may be summarized briefly as follows:

- *Deposition.* Particles are deposited on the surface, which causes buildup in the profile. The particles may either isotropically condense from the surroundings (known as chemical or “wet” deposition) or be deposited from a source. The main advantage of this latter technology is increased control over the directionality of surface deposition. The rate of deposition and, hence, growth of the layer may depend on source masking, visibility effects between the source and surface point, angle-dependent flux distribution of source particles, the angle of incidence of the particles relative to the surface normal direction, reflection of source particles, and surface diffusion effects.

- *Etching.* Particles remove material from the evolving profile boundary. The material may be isotropically removed, known again as chemical or “wet” etching, or chipped away through reactive ion etching, also known as “ion milling.” Similar to deposition, the main advantage of reactive ion etching is enhanced directionality, which becomes increasingly important as device sizes decrease substantially and etching must proceed in vertical directions without affecting adjacent features. As described in [40], the total etch rate consists of an ion-assisted rate and a purely chemical etch rate due to etching by neutral radicals, which may still have a directional component. As

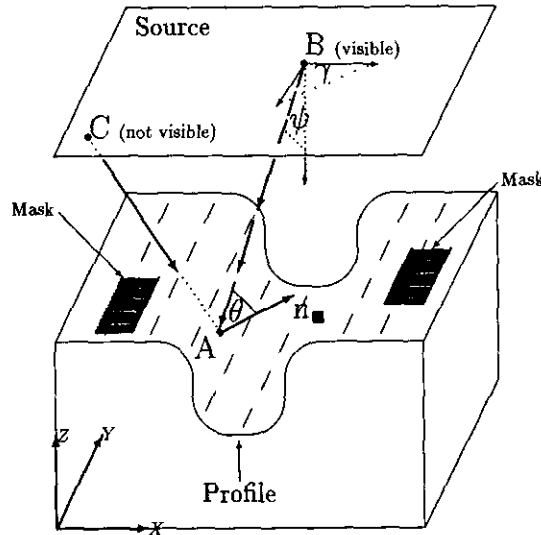


FIG. 5. Variables and setup.

in the above, the total etch rate due to wet and directional milling effects can depend on source masking, visibility effects between the source and surface point, angle-dependent flux distribution of source particles, the angle of incidence of the particles relative to the surface normal direction, reflection/re-emission of etching/milling particles, and surface diffusion effects.

- **Lithography.** The underlying material is treated by an electromagnetic wave which alters the resist property of the material. The aerial image is found, which then determines the amount of crosslinking at each point in the material giving the etch/resist rate at each point of the material. A profile is then etched into the material, where the speed of the profile in the normal direction at any point is given by the underlying etch rate. The key factors that determine the evolving shape are the etch/resist profile and masking effects.

In the rest of this section, we formalize the above.

3.1. Initial Position and Setup

Define the coordinate system with the x and y axis lying in the plane and z being the vertical axis. We consider a periodic initial profile $h(x, y)$, where h gives the height of the initial surface above the xy plane. We also consider a source Z given as a surface above the initial profile and write $Z(x, y)$ referring to the height of the source at the point (x, y) .

For both etching and deposition, define a source ray as leaving the source and aimed towards the surface profile. Let ψ be the angle between the source ray and the negative z axis; ψ runs from 0 to π , though it is physically unreasonable to have ψ values between $\pi/2$ and π . Let γ be the

angle between the projection of the source ray in the xy plane and the positive x axis. Let n be the normal vector at a point x on the surface profile, and θ be the angle between the normal and the source ray.

In Fig. 5, we indicate these variables. Masks, which force flux rates to be zero, are indicated by heavy dark patches on the initial profile. At each point of the profile we assign a visibility indicator function $M_V(\mathbf{x}, \mathbf{x}')$ which indicates whether the point \mathbf{x} on the initial profile can be seen by the source point \mathbf{x}' .

Our goal is to write the effects of deposition, etching, and lithography on the speed F at a point \mathbf{x} on the front.

3.2. Deposition

We consider three separate types of deposition:

- F_{Iso}^D : *Isotropic deposition.* Uniform deposition.
- F_{Uni}^D : *Unidirectional deposition.* Deposition in a particular direction, based on the angle of the incoming stream.
- F_{Sou}^D : *Source deposition.* Deposition radiating from a point source, including sputter deposition and angle-based flux functions.

In Fig. 5, we generalize the latter two effects as the "source." Thus, the source as shown in the figure may consist of locations which emit either unidirectional deposition or point source deposition.

The above terms may be assembled as

$$F_{\text{Deposition}} = F_{\text{Deposition}} (F_{\text{Iso}}^D, F_{\text{Uni}}^D, F_{\text{Sou}}^D); \quad (16)$$

that is, the deposition speed may depend on isotropic, unidirectional, or source deposition.

Let $M_Y(\mathbf{x}, \mathbf{x}')$ be one if the point \mathbf{x}' on the source is visible from the point \mathbf{x} on the profile, and zero otherwise. Let r be the distance from \mathbf{x} to \mathbf{x}' , and, finally, let α be the unit vector at the point \mathbf{x}' on the source pointing towards the point \mathbf{x} on the profile. Then we may refine the above terms.

3.2.1. Isotropic Deposition

$$F_{\text{Iso}}^D = R_{\text{Iso}}^D \text{Flux}_{\text{Iso}}^D. \quad (17)$$

Here, R_{Iso}^D is the rate of growth and $\text{Flux}_{\text{Iso}}^D(\mathbf{x})$ is the isotropic flux function.

3.2.2. Unidirectional Deposition

$$F_{\text{Uni}}^D = -R_{\text{Uni}}^D(\mathbf{x})M_Y(\mathbf{x}, \mathbf{x}')\text{Flux}_{\text{Uni}}^D(r, \psi, \gamma, \theta, \mathbf{x})(\mathbf{n} \cdot \alpha). \quad (18)$$

Here, R_{Uni}^D is the rate of growth, and $\text{Flux}_{\text{Uni}}^D(r, \psi, \gamma, \theta, \mathbf{x})$ is the unidirectional flux function, which may depend on the distance r , the emission angles ψ and γ , the angle of incidence θ , and the starting point \mathbf{x} .

3.2.3. Source Deposition

$$F_{\text{Sou}}^D = -R_{\text{Sou}}^D(\mathbf{x}) \int_{\text{Source}} \text{Flux}_{\text{Sou}}^D(r, \psi, \gamma, \theta, \mathbf{x}) \times M_Y(\mathbf{x}, \mathbf{x}')(\mathbf{n} \cdot \alpha) d\sigma. \quad (19)$$

Here, the integral is over the entire source, R_{Sou}^D is the rate of growth, and $\text{Flux}_{\text{Sou}}^D(r, \psi, \gamma, \theta, \mathbf{x})$ is the flux function. A typical flux function might include the effects of sputter deposition and be of the form $\cos^n(A\psi)$, where n is a constant and $|\psi| \leq 2\pi A$.

3.3. Etching

In this formulation, the equations of etching are quite similar; we include them for the sake of completeness. We consider three separate types of etching:

- F_{Iso}^E : *Isotropic etching*. Uniform etching. This may be a function of the underlying material.
- F_{Uni}^E : *Unidirection etching*. Etching in a particular direction, based on the angle of the incoming stream.
- F_{Sou}^E : *Source deposition*. Etching radiating from a point source, including ion-milling and transport of neutral radicals.

The above terms may be assembled as

$$F_{\text{Etching}} = F_{\text{Etching}}(F_{\text{Iso}}^E, F_{\text{Uni}}^E, F_{\text{Sou}}^E), \quad (20)$$

where again we may refine the above terms.

3.3.1. Isotropic Etching

$$F_{\text{Iso}}^E = -R_{\text{Iso}}^E \text{Flux}_{\text{Iso}}^E. \quad (21)$$

Here, R_{Iso}^E is the etch rate based on the isotropic flux function $\text{Flux}_{\text{Iso}}^E(\mathbf{x})$.

3.3.2. Unidirectional Etching

$$F_{\text{Uni}}^E = R_{\text{Uni}}^E(\mathbf{x})M_Y(\mathbf{x}, \mathbf{x}')\text{Flux}_{\text{Uni}}^E(r, \psi, \gamma, \theta, \mathbf{x})(\mathbf{n} \cdot \alpha). \quad (22)$$

Here, R_{Uni}^E is the etch rate, and $\text{Flux}_{\text{Uni}}^E(r, \psi, \gamma, \theta, \mathbf{x})$ is the unidirectional flux function, which may depend on the distance r from \mathbf{x} to the source, the emission angles ψ and γ , the angle of incidence θ , and the starting point \mathbf{x} .

3.3.3. Source Etching

$$F_{\text{Sou}}^E = R_{\text{Sou}}^E(\mathbf{x}) \int_{\text{Source}} \text{Flux}_{\text{Sou}}^E(r, \psi, \gamma, \theta, \mathbf{x}) \times M_Y(\mathbf{x}, \mathbf{x}')(\mathbf{n} \cdot \alpha) d\sigma. \quad (23)$$

Here, the integral is over the entire source. R_{Sou}^E is the rate of growth, and $\text{Flux}_{\text{Sou}}^E(r, \psi, \gamma, \theta, \mathbf{x})$ is the flux function.

3.4. Lithography

The construction of the speed function for lithographic cases is straightforward if one assumes that the etch rate is given. Typically, an aerial image is found using a simulator such as SPLAT [43], which, together with a program such as BLEACH [43], provides the etch rate at each point of the material. Since the etch rate is provided everywhere in the material, we may simply write

$$F_{\text{Lithography}} = -R_{\text{Litho}}, \quad (24)$$

where the etch rate R_{Litho} is supplied by the simulator.

3.5. Other Effects

In etching and deposition, additional effects can play an important role in the evolving profile. These include:

- *Surface migration*. Particles can migrate when they collide with the interface. This causes a diffusion-like term which tends to diffuse large peaks of velocities. Given the above speed function F for surface motion, one can think of two ways to include the effects of surface diffusion/migration. One is to simply modify the speed function by the term $1 - \varepsilon K$, where K is the local curvature, which has the effect of diffusing the front. The second way is to obtain a more accurate representation of the diffusion term as follows. Given a surface $x(s)$ in R^2 , we imagine that a

scalar function g is defined on that surface, and solve the diffusion equation $g_t = \epsilon \nabla^2 g$ along the surface.

- *Re-emission/reflection.* Some of incoming flux/neutral radicals may not stick to the surface, but instead be reflected/re-emitted. The fraction of particles that are not reflected/re-emitted is known as the “sticking probability” and varies between 0 and 1. Thus, a sticking probability of unity corresponds to the case under study above. For sticking probabilities less than unity and depending on the surface physics, the re-emission can be either specular or diffusive. Thus, each point on the evolving profile may act as additional source when viewed from other visible sites on the front. This can be set up as an integral equation for the total source flux at a point, depending on the seen visible angle and probability flux re-emission distribution. For details, see the derivation in [40] and the calculations in [24]. This integral is discretized by a dense, non-symmetric matrix which must be solved at each time step in order to calculate the correct flux to advance the front. In two dimensions this is tractable; in three dimensions, the problem is daunting and requires significant resources. Extensions of the level set approach to problems including reflection, reemission, and surface diffusion are the focus of Part III of this paper [3].

4. FUNDAMENTAL IDEAS OF IMPLEMENTATION

We briefly discuss the application of the level set approach to this problem. Complete details may be found in Part I [2] of this sequence.

Rather than employ the full level set approach, we use a narrow band version which focusses computational labor on cells which bracket the zero-level set corresponding to the front. This approach was introduced in [8], used in recovering images in [22], and analyzed extensively in [1]. There are two reasons to do so. The first is speed; in three dimensions, the operation count for the full level set method is $O(N^3)$, where N is the number of cells in each direction. By limiting calculations to a narrow band of width k around the zero-level set, the operation count drops to $O(kN^2)$, which is a substantial savings. Typically we use bandwidths of six cells in each direction, and the corresponding speedup is an order of magnitude over the full level-set approach.

The second reason to employ the narrow band construction is because certain properties of the front which contribute to determining its motion have no natural meaning on other level sets. For example, the visibility of the front has meaning for the zero-level set, but not for others. Such variables, known as extension variables, are best treated by the following approach: for any given level set, the value of the extension variable is found by using the value on the closest point of the zero level set. For details, see [1, 2].

Local variables, such as normal vectors and curvature

have meaning for all the level sets and may be easily calculated using those values. Normals are calculated using the average one-sided difference technique. Variations in etch rate, either through masks, material dependence, or lithographic etch rates are directly incorporated into the speed function.

The front is updated using second order in space schemes specially designed for the level-set function; see [2]. There are two separate schemes; first, an ENO-based scheme for convex speed functions F which most naturally occur in lithography simulations and some source deposition problems, and a non-convex Lax–Friedrichs/ENO scheme (see [27]) which can be required for sputter etch/deposition problems. In three space dimensions, the schemes are given by:

1. First-order space convex.

$$\phi_{ijk}^{n+1} = \phi_{ijk}^n - \Delta t [\max(F_{ij}, 0) \nabla^+ + \min(F_{ij}, 0) \nabla^-], \quad (25)$$

where

$$\begin{aligned} \nabla^+ = & [\max(D_{ijk}^{-x}, 0)^2 + \min(D_{ijk}^{+x}, 0)^2 \\ & + \max(D_{ijk}^{-y}, 0)^2 + \min(D_{ijk}^{+y}, 0)^2 \\ & + \max(D_{ijk}^{-z}, 0)^2 + \min(D_{ijk}^{+z}, 0)^2]^{1/2} \end{aligned} \quad (26)$$

$$\begin{aligned} \nabla^- = & [\max(D_{ijk}^{+x}, 0)^2 + \min(D_{ijk}^{-x}, 0)^2 \\ & + \max(D_{ijk}^{+y}, 0)^2 + \min(D_{ijk}^{-y}, 0)^2 \\ & + \max(D_{ijk}^{+z}, 0)^2 + \min(D_{ijk}^{-z}, 0)^2]^{1/2}. \end{aligned} \quad (27)$$

2. *Second-order space convex.* The same as the above, however, where this time ∇^+ and ∇^- are given by

$$\begin{aligned} \nabla^+ = & [\max(A, 0)^2 + \min(B, 0)^2 \\ & + \max(C, 0)^2 + \min(D, 0)^2 \\ & + \max(E, 0)^2 + \min(F, 0)^2]^{1/2} \end{aligned} \quad (28)$$

$$\begin{aligned} \nabla^- = & [\max(B, 0)^2 + \min(A, 0)^2 \\ & + \max(D, 0)^2 + \min(C, 0)^2 \\ & + \max(F, 0)^2 + \min(E, 0)^2]^{1/2}, \end{aligned} \quad (29)$$

where

$$A = D_{ijk}^{-x} + \frac{\Delta x}{2} m(D_{ijk}^{-x-x}, D_{ijk}^{+x-x}) \quad (30)$$

$$B = D_{ijk}^{+x} - \frac{\Delta x}{2} m(D_{ijk}^{+x+x}, D_{ijk}^{+x-x}) \quad (31)$$

$$C = D_{ijk}^{-y} + \frac{\Delta y}{2} m(D_{ijk}^{-y-y}, D_{ijk}^{+y-y}) \quad (32)$$

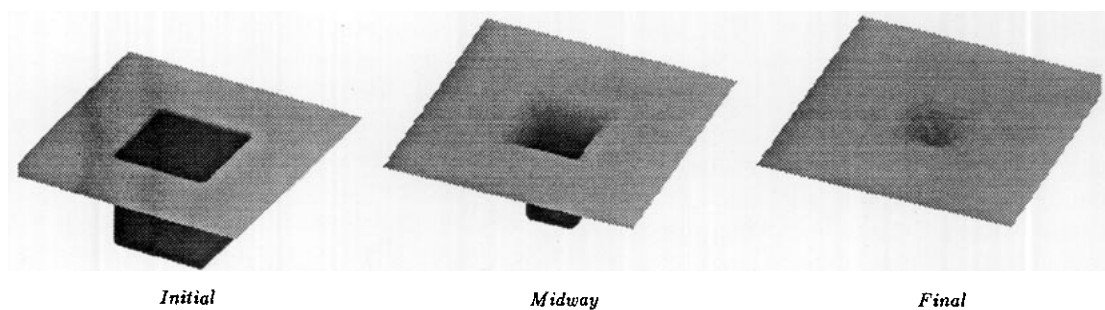


FIG. 6. Isotropic deposition into hole.

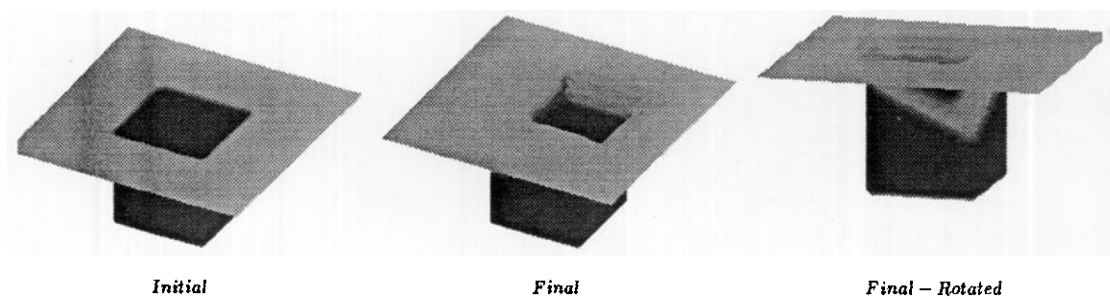


FIG. 7. Directional deposition into hole.

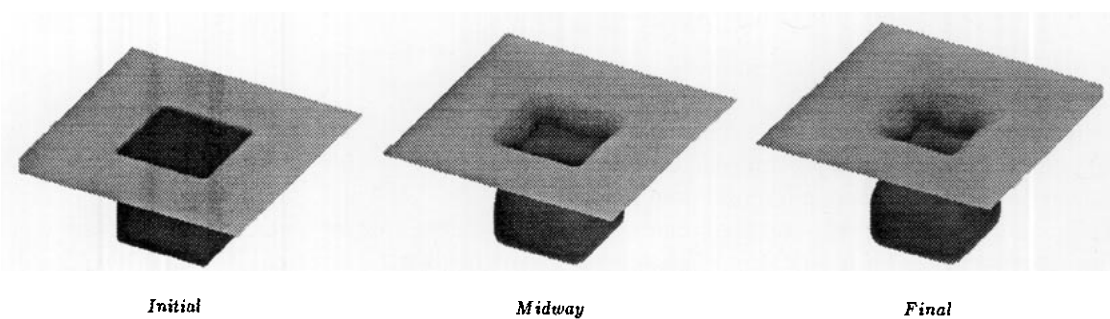


FIG. 8. Source deposition into hole.

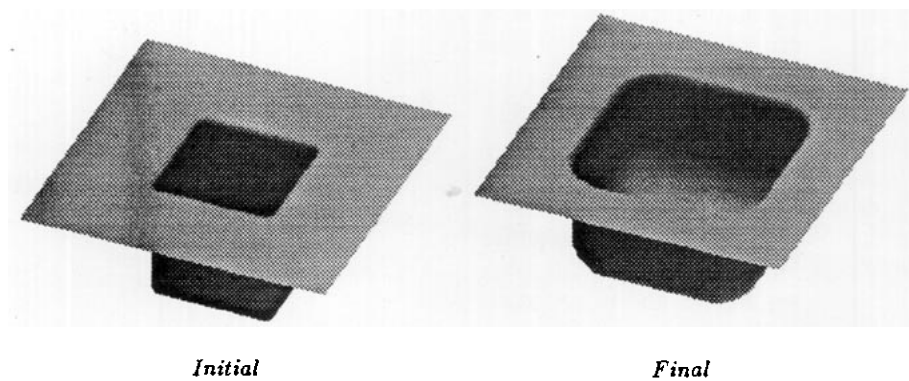


FIG. 9. Isotropic etching into hole.

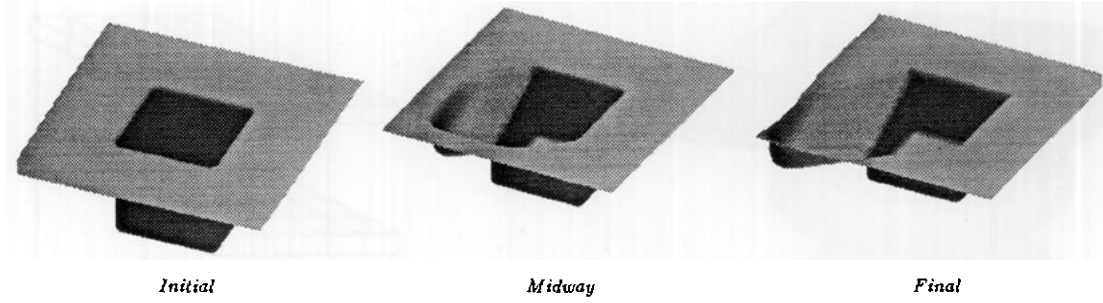


FIG. 10. Directional etching into hole.

$$D = D_{ijk}^{+y} - \frac{\Delta y}{2} m(D_{ijk}^{+y+y}, D_{ijk}^{+y-y}) \quad (33)$$

$$E = D_{ijk}^{-z} + \frac{\Delta z}{2} m(D_{ijk}^{-z-z}, D_{ijk}^{+z-z}) \quad (34)$$

$$F = D_{ijk}^{+z} - \frac{\Delta z}{2} m(D_{ijk}^{+z+z}, D_{ijk}^{+z-z}) \quad (35)$$

and the switch function is given by

$$m(x, y) = \begin{cases} x & \text{if } |x| \leq |y| \\ y & \text{if } |x| > |y| \\ 0 & xy < 0. \end{cases} \quad (36)$$

3. First-order space non-convex.

$$\begin{aligned} \phi_{ijk}^{n+1} = \phi_{ijk}^n - \Delta t \left[H \left(\frac{D_{ijk}^{-x} + D_{ijk}^{+x}}{2}, \frac{D_{ijk}^{-y} + D_{ijk}^{+y}}{2}, \frac{D_{ijk}^{-z} + D_{ijk}^{+z}}{2} \right) \right. \\ \left. - \frac{1}{2} \alpha_u (D_{ijk}^{+x} - D_{ijk}^{-x}) - \frac{1}{2} \alpha_v (D_{ijk}^{+y} - D_{ijk}^{-y}) \right. \\ \left. - \frac{1}{2} \alpha_w (D_{ijk}^{+z} - D_{ijk}^{-z}) \right], \end{aligned} \quad (37)$$

where M_u (M_v , M_w) is a bound on the partial derivative of the Hamiltonian with respect to the first (second, third) argument, and the non-convex Hamiltonian is a user-defined input function.

4. Second-order space non-convex.

$$\phi_{ijk}^{n+1} = \phi_{ijk}^n - \Delta t \left[H \left(\frac{A+B}{2}, \frac{C+D}{2}, \frac{E+F}{2} \right) \right] \quad (38)$$

$$\begin{aligned} - \frac{1}{2} M_u (B - A) - \frac{1}{2} M_v (D - C) \\ - \frac{1}{2} M_w (F - E) \end{aligned} \quad (39)$$

where A , B , C , D , E , and F are defined as above.

5. *Time integration.* The above is for first-order explicit schemes. The most natural way to make a second order in time version is through a predictor/corrector method, e.g., Heun's method. This requires embedding the entire sequence of one time step advancement in a two-step loop. More precisely, proceed as follows:

(a) Let $\phi_{ijk}^{(n+1)*}$ be the solution obtained by updating the solution ϕ_{ijk}^n one time step.

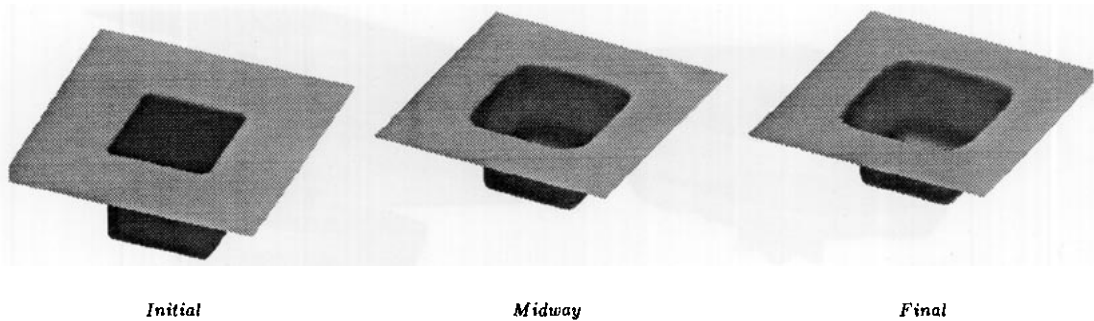


FIG. 11. Source etching into hole.

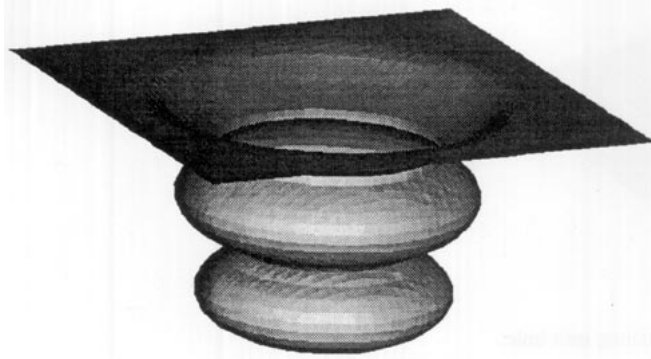


FIG. 12. Lithographic Development.

(b) Let $\phi_{ijk}^{(n+2)**}$ be the solution obtained by updating the solution $\phi_{ijk}^{(n+1)*}$ one time step.

(c) Then let

$$\phi_{ijk}^{n+1} = \phi_{ijk}^n + 0.5[\phi_{ijk}^{(n+2)**} - \phi_{ijk}^n]. \quad (40)$$

5. NUMERICAL TESTS OF METHOD

In this section, we perform some tests to demonstrate the power of this approach.

5.1. Deposition

5.1.1. Isotropic Deposition

We begin by studying isotropic deposition. This is fairly straightforward application of the level-set approach. In Fig. 6 we show a square hole upon which a material is being isotropically deposited; this corresponds to a simple

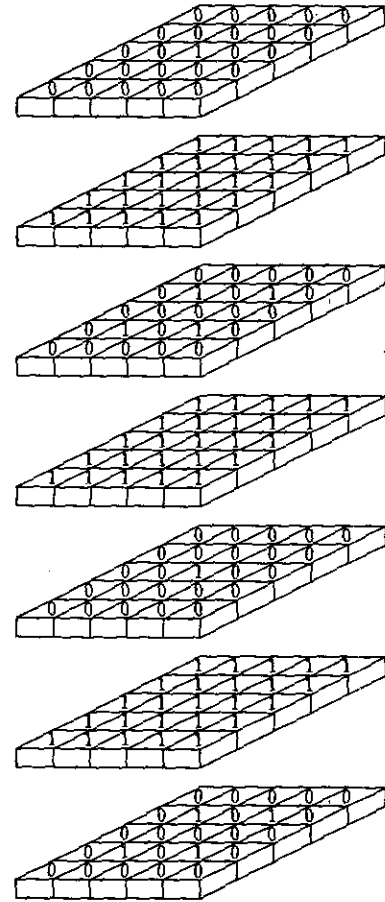


FIG. 13. Layering of discontinuous etch coefficients.

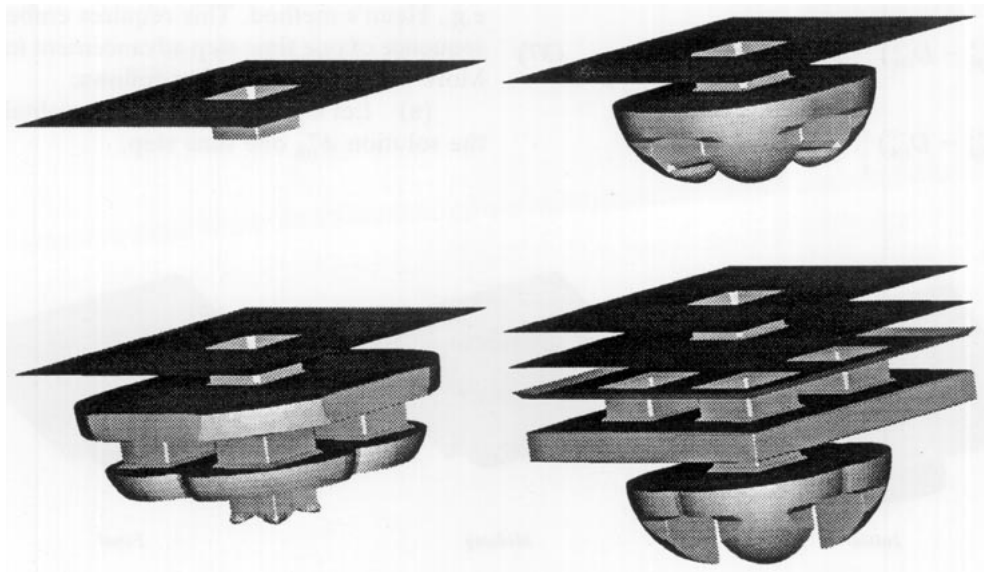


FIG. 14. Etching profile through multiblocks.

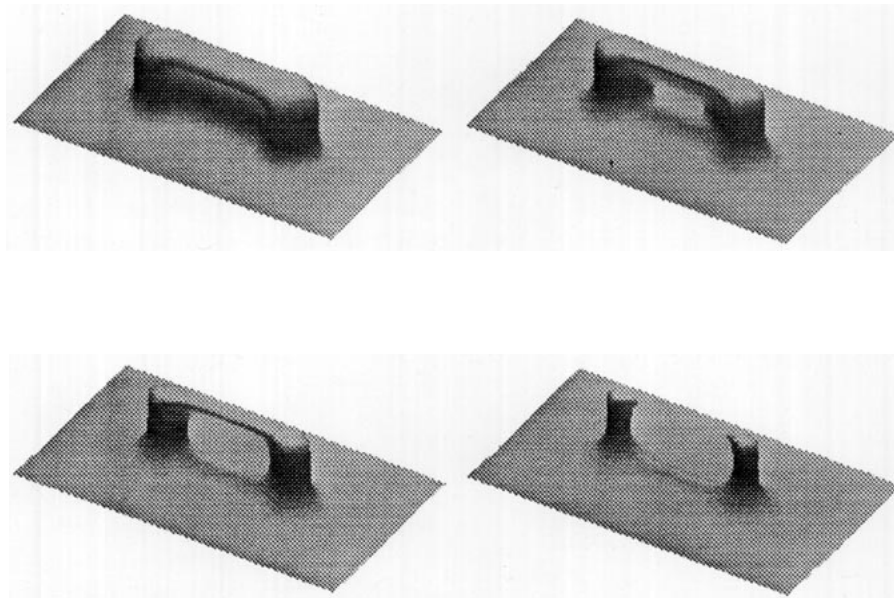
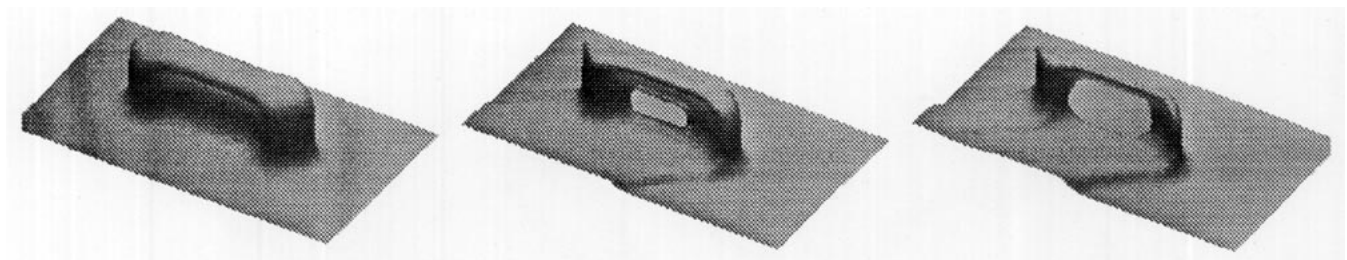


FIG. 15. Isotropic etching of bridge.

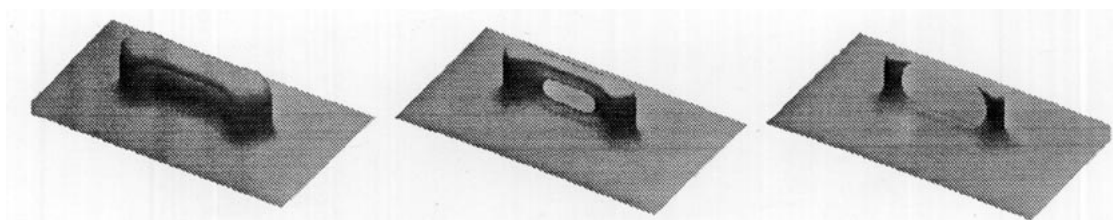


Initial

Midway

Final

FIG. 16. Unidirectional etching of bridge.



Initial

Midway

Final

FIG. 17. Source etching of bridge.

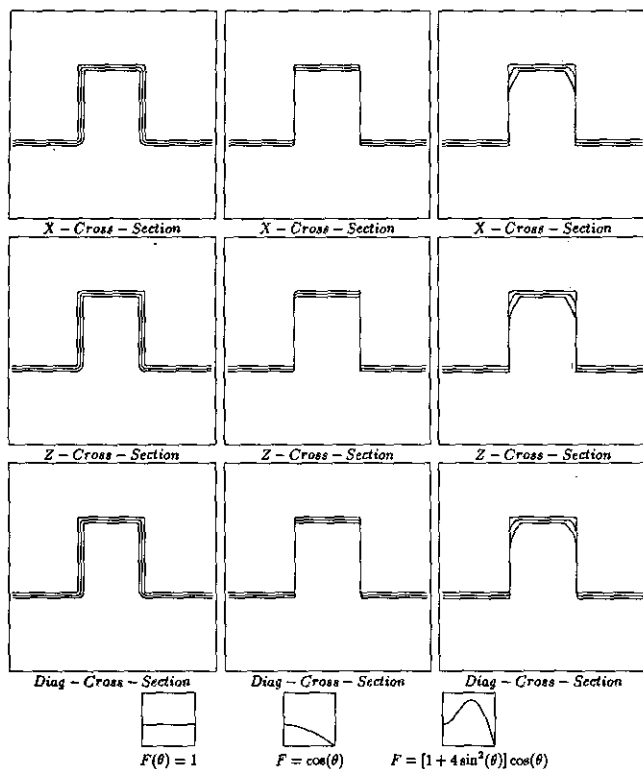


FIG. 18. Three dimensions: Effects of different yield functions.

speed function of $F = 1$. The hole closes off as the deposition material fills in the cavity.

5.1.2. Directional Deposition

We next study isotropic deposition. We consider directional deposition from a plane located above a square hole, where the effects of visibility and shading are included. In Fig. 7, we show two three-dimensional plots which show the evolving profile. The slant of the profile in the direction of the directional deposition source is clearly seen; note in particular the shearing below the surface in the rotated figure.

5.1.3. Source Deposition

Finally, we study source deposition. We consider source deposition from a plane located above the hole. Again, the effects of visibility and shading are included. Along the entire plate, deposition material is emitted uniformly in each direction. In Fig. 8, we show two three-dimensional time plots of the evolving profile. The trench begins to pinch off due to the effects of visibility, and a bulb-shaped profile evolves.

5.2. Etching

We now repeat the above experiments under the effects of various types of etching.

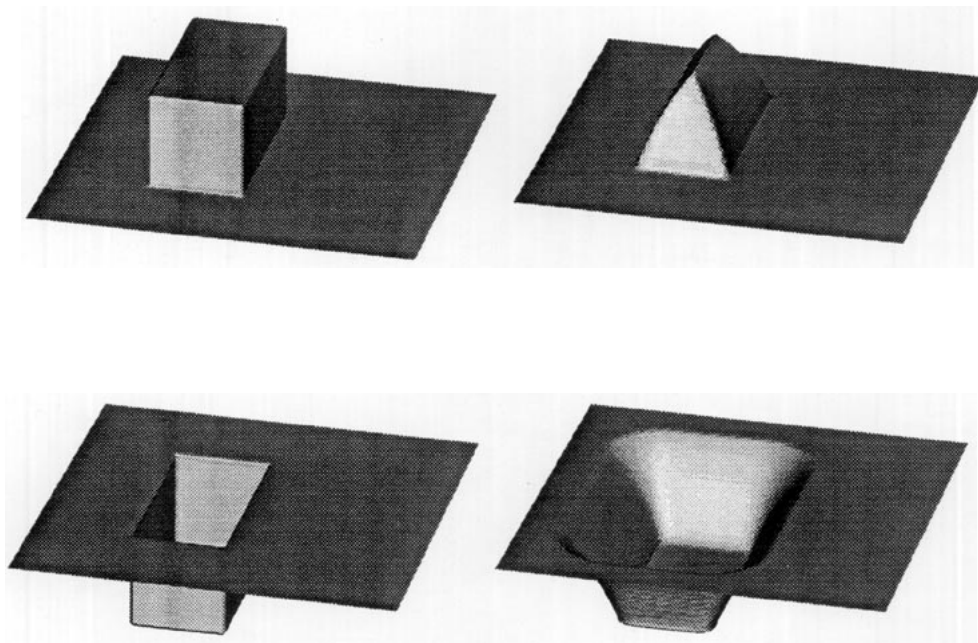


FIG. 19. Rectangular peg and hole under sputter etch.

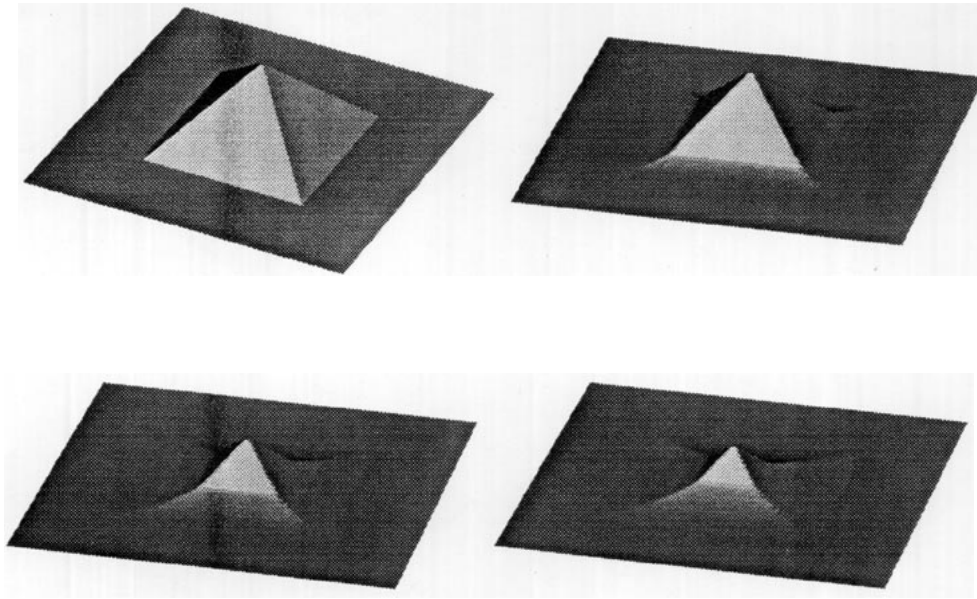


FIG. 20. Pyramid under sputter etch.

5.2.1. Isotropic Etching

First, we study isotropic etching. In Fig. 9 we show a square hole from which a material is being isotropically etched; this corresponds to a simple speed function of $F = -1$. As expected, the sides of the cavity are cleanly etched away, leaving smoothed, rounded walls.

5.2.2. Directional Etching

Next, we study directional etching. We consider directional etching from a plane located above a cavity, where the effects of visibility and shading are included. In Fig. 10, we show a sequence of three-dimensional time

plots which show the evolving profile. The etching direction is on the upper right in the figure; the etching beam shears away the profile on the left first, and then as the shadowing wall is eaten away, it continues to shear the left side of the profile.

5.2.3. Source Etching

Finally, we study source etching. We consider source etching from a plane located above a cavity. Again, the effects of visibility and shading are included. Along the entire plane, etching rays are uniformly distributed. In Fig. 11, we show a sequence of three-dimensional time plots

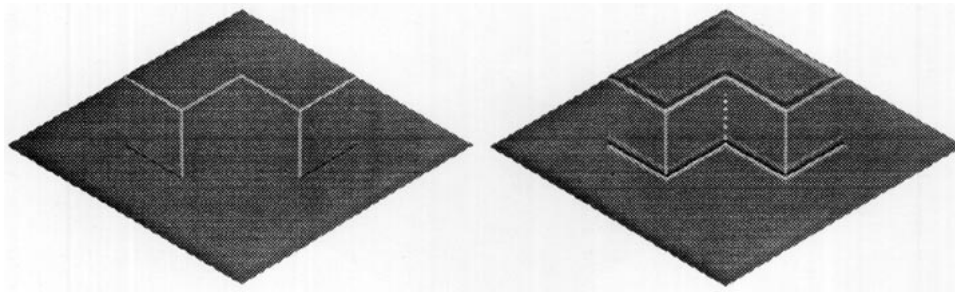


FIG. 21. Upward saddle under sputter etch.

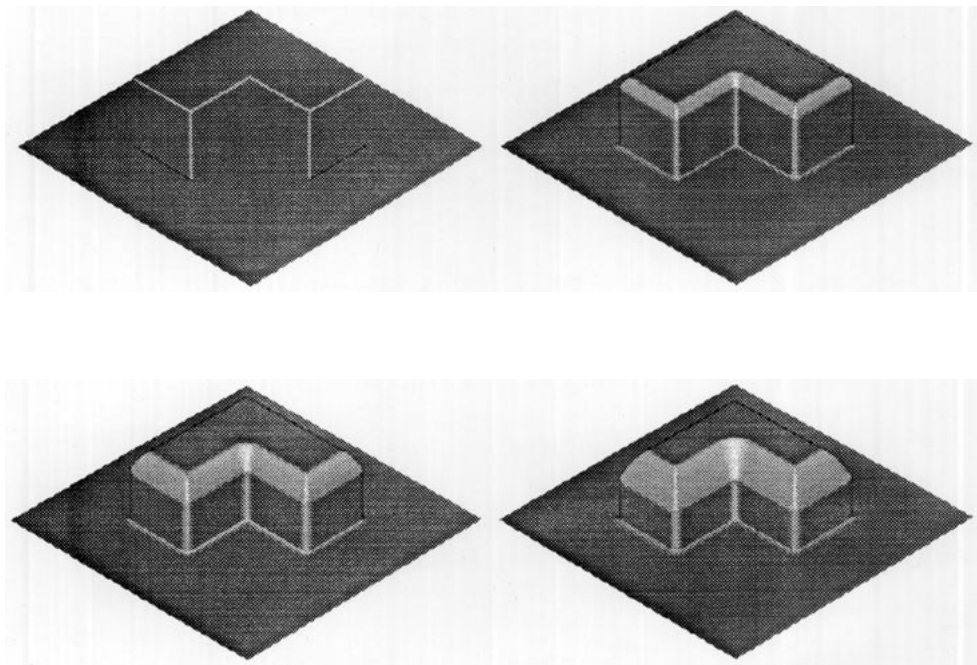


FIG. 22. Upward saddle under sputter etch.

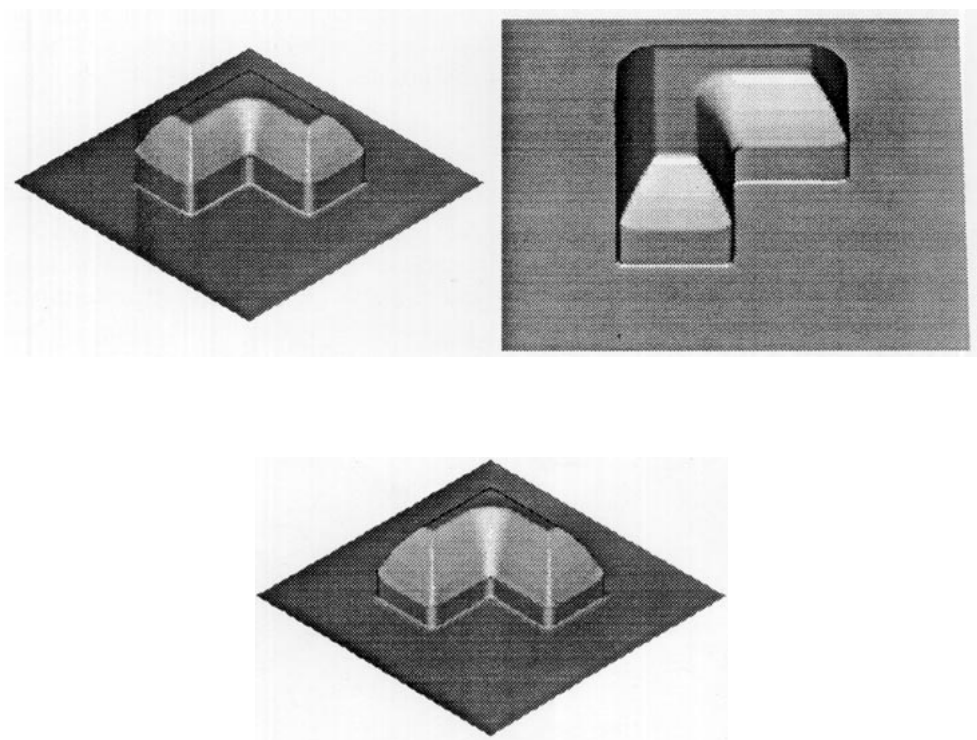


FIG. 23. Upward saddle under sputter etch.

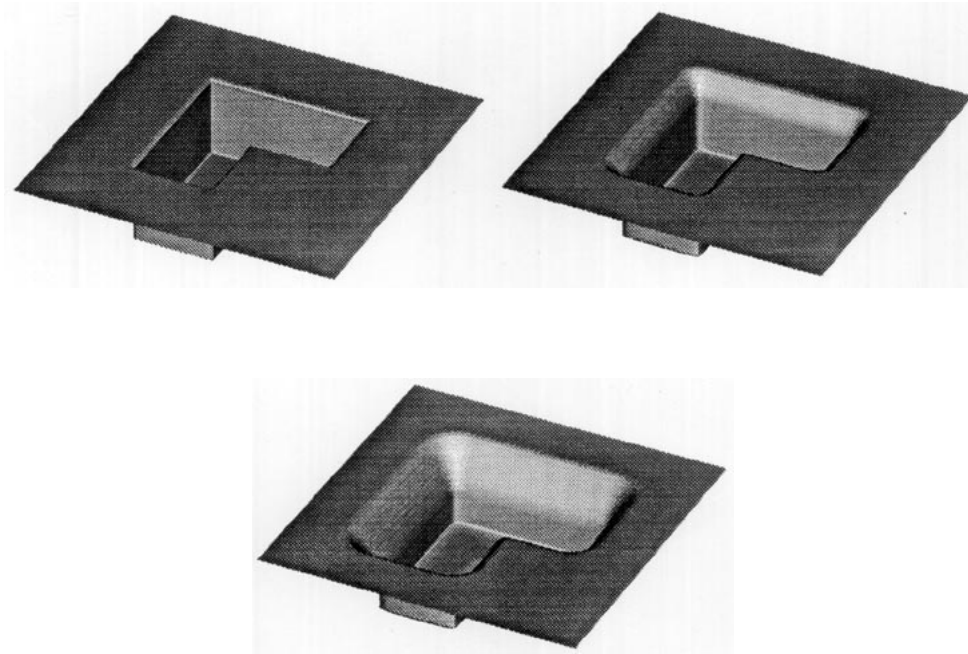


FIG. 24. Downward saddle under sputter etch.

which show the evolving profile. The fact that visibility is included keeps the walls of the profile fairly steep, in contrast with the isotropic case shown earlier.

5.3. Lithography

Next, we perform a lithographic etch, in which the rate function is obtained from other numerical simulations; see [43]. We use a second-order method with a grid size of $50 \times 50 \times 47$. In Fig. 12, results of the evolving profile are shown.

6. SOME MODEL PROBLEMS

In this section, we perform a series of additional experiments to demonstrate the versatility of the level set approach.

6.1. Etching under Discontinuous Etch Coefficients

First, we show what happens when an etching front propagates into a material with discontinuous etch coefficients. These discontinuous coefficients cause sharp edges and corners in the etch profile. We imagine a multilayered material, with etch coefficients of either zero or one. The etch distribution is given in Fig. 13, while the evolution of the planar profile down through this material structure is given in Fig. 14. The side walls of the first sub-layer are removed in the final figure to show the hidden downward cavities.

6.2. Development of Topological Changes in Profiles: Etching and Deposition

Next, we consider initial profiles which lend themselves to topological changes as they evolve.

We begin by studying isotropic etching of a bridge. The bridge initial has a thin curtain stretched underneath it; the thickness of the curtain is smallest at the middle (see Fig. 15a). In Fig. 15, we show the evolution of this bridge under isotropic etching. The results show first the disintegration of the curtain at its center, followed by the narrowing of the top and the final image of two independent pillars being etched away.

Next, in Fig. 16, we show the same structure under unidirectional etching. Here, the pillars shadow the profile, and their effect can be seen on the flat part of the surface. The bridge is again etched away.

Finally, in Fig. 17, we consider the evolution of the above bridge structure under source etching. We compare this case with the isotropic case; because the etching stream is coming almost uniformly from the source plate, the main difference lies in the shadowing effects below the bridge.

6.3. Sputter Etching/Deposition

As discussed extensively in Part I, in some sputter problems (for example, ion milling), the normal speed of the profile depends on the angle of incidence between the

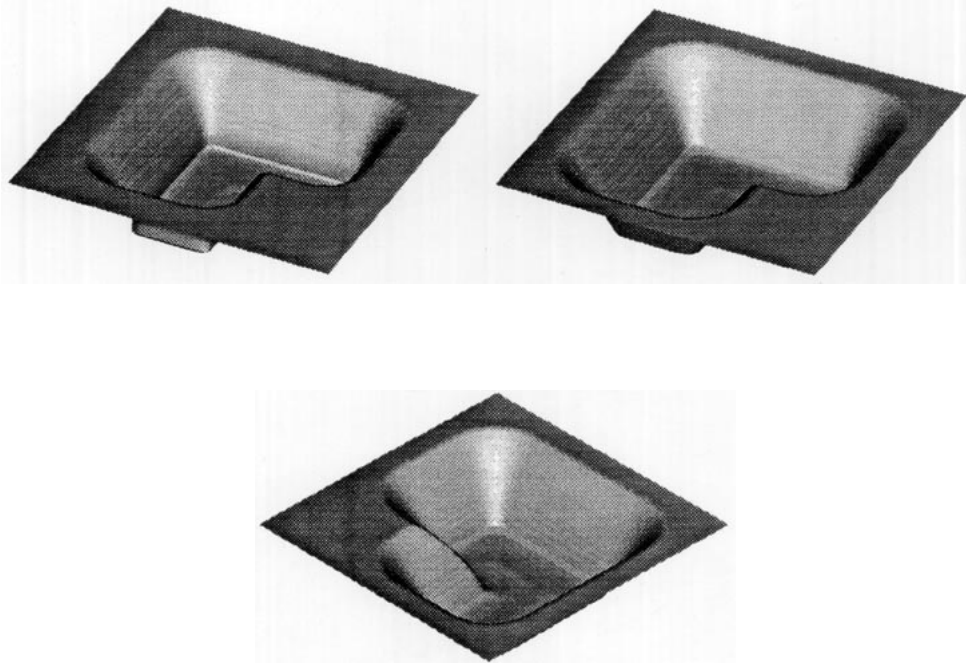


FIG. 25. Downward saddle under sputter etch.

surface normal and the incoming ray. This yield function is often empirically fit from experiment and has been observed to cause such effects as faceting at corners; see [21, 18]. The resulting equation of motion for the speed function F yields a non-convex Hamiltonian, which then must be approximated using non-convex schemes. In the simulations below, we employ the non-convex Lax-Friedrichs scheme given above.

We envision a ray coming down in the vertical direction. In all cases under study here, the angle θ shown in Fig. 5 refers to the angle between the surface normal and the positive vertical. For this set of calculations, in order to examine the geometry of sputter effects on shocks/rarefaction fan development, we ignore visibility effects. Following our usual notation, let $F(\theta)$ be the speed of the front in a direction normal to the surface.

In Fig. 18, we show two-dimensional cross sections of a three-dimensional square cap being etched away. In column A we show the effects of purely isotropic motion; thus the yield function is $F = 1$. The top row gives the x cross section, the second row the y cross section, and the third row is the diagonal cross section. Located in the last row is the etch function F as a function of angle θ ; hence for this case $F = 1$ and the line is flat. In column B we show the effects of directional motion; thus the yield function is $F = \cos(\theta)$. Vertical lines of the profile do not move, and horizontal components

move with unit speed. In column C we show the effects of a yield function suggested by Leon [20] of the form $F = [1 + 4 \sin^2(\theta)] \cos(\theta)$.

The results show that the effects of angle-dependent yield functions are pronounced. In column A the isotropic rate produces smooth corners, correctly building the necessary rarefaction fans in outward corners and entropy-satisfying shocks in the inward corners as discussed and analyzed in [33, 34]. In column B, the directional rate causes the front to be essentially translated downwards, with minimal rounding of the corners. In column C, the yield function results in faceting of inward corners, where shocks form, and sharp translations of the side walls in the direction of the etch. A comparison of this profile with the “exact” solution as predicted using the method of characteristics is given in Part I of this paper [2].

In the final set of examples, we show a collection of three-dimensional etching simulations under this non-convex sputter law $F = [1 + 4 \sin^2(\theta)] \cos(\theta)$. We begin with Fig. 19 showing etching of a rectangular peg and hole.

Next, we show etching under the same speed function of a pyramid; here the different facets meet at a point. As the figure is etched away, the non-convex speed function promotes “ribbing” of the evolving profile, as seen in Fig. 20.

Next, we show the effects of etching on extruding and

excavated shapes containing sharp corners and saddle points. We start with an upward saddle surface under the sputter etch function

$$F = [1 + A \sin^2(\theta)] \cos(\theta). \quad (41)$$

In Figs. 21, 22, and 23, we study the effects under $A = 0$ and $A = 4$.

Finally, we study the same etching laws applied to an indented saddle surface, as shown in Figs. 24 and 25.

7. SUMMARY

The numerical method presented in this paper can be used for a wide variety of three-dimensional simulations in etching, deposition, and lithography; the method naturally takes into account such effects as incident angles, masks, yield functions, visibility, and anisotropy on the surface motion. Due to the use of conservative upwind schemes, the method selects the correct entropy condition and maintains sharp corners where shocks in the tangent occur; conversely, the correct rarefaction fan solution is built at outward-facing corners. The method is second-order accurate in space and time in the motion of the front. By using the narrow band approach, the method is of the same computational work as cell and marker particle methods; that is, the work is a constant times the number of points which characterize the evolving front. In Part III [3], we present the extension of this work to include effects of reflection, re-emission, and surface diffusion. Finally, in [38] we present an extremely fast marching level set method based on control theory and sorting, and applicable to lithography development and some problems in etching and deposition.

ACKNOWLEDGMENTS

All calculations were performed at the University of California at Berkeley and the Lawrence Berkeley Laboratory. We thank B. Coughran, J. Helmsen, J. Lee, P. Leon, A. Neureuther, C. Rafferty, J. Rey, V. Singh, K. Smith, and K. Toh for helpful discussions.

REFERENCES

1. D. Adalsteinsson and J. A. Sethian, *J. Comput. Phys.* **118** (1995), 269.
2. D. Adalsteinsson and J. A. Sethian, *J. Comput. Phys.* **120** (1995), 128.
3. D. Adalsteinsson and J. A. Sethian, in progress.
4. S. Altschuler, S. B. Angenent, and Y. Giga, preprint, 1993.
5. A. Bourlioux and J. A. Sethian, to be submitted, 1995.
6. Y. C. Chang, T. Y. Hou, B. Merriman, and S. J. Osher, *J. Comput. Phys.*, to appear.
7. Y. Chen, Y. Giga, and S. Goto, *J. Differential Geom.* **33**, 749 (1991).
8. D. L. Chopp, *J. Comput. Phys.* **106**, 77 (1993).
9. D. L. Chopp and J. A. Sethian, *J. Exp. Math.* **2**, 235 (1993).
10. L. C. Evans, H. M. Sonar, and P. E. Souganidis, *Commun. Pure Appl. Math.* **45**, 1097 (1992).
11. L. C. Evans and J. Spruck, *J. Differential Geom.* **33**, 635 (1991).
12. L. C. Evans and J. Spruck, *Trans. Am. Math. Soc.* **330**, 91 (1992).
13. M. Falcone, T. Giorgi, and P. Loretti, Istituto per le Applicazioni del Calcolo, Rome, preprint, 1990.
14. Y. Giga and S. Goto, *J. Math. Soc. Jpn.* **44**, 99 (1992).
15. M. Grayson, *J. Differential Geom.* **26**, 285 (1987).
16. J. J. Helmsen and A. R. Neureuther, "3D Lithography Cases for Exploring Technology Solutions and Benchmarking Simulators," in *Optical/Laser Microlithography VI*, SPIE, Vol. 1927, p. 382-394, (Int. Soc. Opt. Eng., Bellingham, WA, 1993).
17. Huiskes, G. *J. Differential Geom.* **20**, 237 (1984).
18. I. V. Katardjiev, G. Carter, and M. J. Nobes, *J. Vac. Sci. Technol. A* **6**(4), 2443 (1988).
19. R. Kimmel and A. Bruckstein, Center for Intelligent Systems Report No. 9209, Technion-Israel Institute of Technology, June 1992 (unpublished).
20. F. A. Leon, personal communication, 1994.
21. F. A. Leon, S. Tazawa, K. Saito, A. Yoshii, and D. L. Scharfetter, "Numerical Algorithms for Precise Calculation of Surface Movement in 3-D Topography Simulation," in *1993 International Workshop on VLSI Process and Device Modeling (1993 VPAD)*.
22. R. Malladi, J. A. Sethian, and B. C. Vemuri, *IEEE Trans. on Pattern Analysis and Machine Intelligence* **17**, 158 (1995).
23. J. P. McVittie, J. C. Rey, A. J. Bariya, and others, *Proc. SPIE* **1392**, 126 (1991).
24. J. P. McVittie, J. C. Rey, L. Y. Cheng, and M. M. IslamRaja, "LPCVD Profile Simulation Using a Re-emission Model," in *International Electron Devices Meeting 1990*. (Technical Digest, IEEE, New York, 1990), p. 917.
25. W. Mulder, S. J. Osher, and J. A. Sethian, *J. Comput. Phys.* **100**, 209 (1992).
26. S. Osher, and J. A. Sethian, *J. Comput. Phys.* **79**, 12 (1988).
27. S. Osher, and C. Shu, *J. Comput. Phys.* **28**, 907 (1991).
28. J. C. Rey, Lie-Yea Cheng, J. P. McVittie, and K. C. Saraswat, *J. Vac. Sci. Technol. A* **9**(3), Part 1, 1083 (1991).
29. C. Rhee, L. Talbot, and J. A. Sethian, *J. Fluid Mech.* **300**, 87 (1995).
30. E. W. Scheckler, Ph.D. dissertation, EECS, University of California, Berkeley, 1991 (unpublished).
31. E. W. Scheckler, K. K. H. Toh, D. M. Hoffstetter, and A. R. Neureuther, "3D Lithography, Etching and Deposition Simulation," in *Symposium on VLSI Technology, Oiso, Japan 1991*, 97 (unpublished).
32. J. A. Sethian, "Algorithms for Tracking Interfaces in CFD and Material Science," in *Computational Fluid Dynamics Review* (Wiley, New York, 1995).
33. J. A. Sethian, Ph.D. dissertation, Mathematics, University of California, Berkeley, 1982 (unpublished).
34. J. A. Sethian, *Commun. Math. Phys.* **101**, 487 (1985).
35. J. A. Sethian, *J. Comput. Phys.* **115**, 440 (1994).
36. J. A. Sethian, *J. Differential Geom.* **31**, 131 (1990).
37. J. A. Sethian, "Numerical Methods for Propagating Fronts," in *Variational Methods for Free Surface Interfaces*, edited by P. Concus and R. Finn (Springer-Verlag, New York, 1987).
38. J. A. Sethian, in progress.
39. J. A. Sethian and J. D. Strain, *J. Comput. Phys.* **98**, (1992).
40. V. K. Singh, S. G. Shaqfeh, and J. P. McVittie, *J. Vac. Sci. Technol. B* **10**(3), 1091 (1993).

41. K. K. H. Toh, Ph.D. dissertation, EECS, University of California, Berkeley, 1990 (unpublished).
42. K. K. H. Toh and A. R. Neureuther, "Three-Dimensional Simulation of Optical Lithography," in *Proceedings SPIE, Optical/Laser Microlithography IV*, 1991, Vol. 1463, p. 356.
43. M. S. Young, D. Lee, R. Lee, and A. R. Neureuther, "Extension of the Hopkins Theory of Partially Coherent Imaging to Include Thin-Film Interference Effects," in *Proc. SPIE Optical/Laser Microlithography VI*, 1993, Vol. 1927, p. 452.
44. J. Zhu and J. A. Sethian, *J. Comput. Phys.* **102**, 128 (1992).